Article:
Liu, Z, Li, Z, Yi, Y et al. (9 more authors) (2022) Flexible strain sensing percolation networks towards complicated wearable microclimate and multi-direction mechanical inputs. Nano Energy, 99. 107444. ISSN 2211-2855

https://doi.org/10.1016/j.nanoen.2022.107444

Flexible strain sensing percolation networks towards complicated wearable microclimate and multi-direction mechanical inputs

Zekun Liu[1], Zhenhong Li[2], Yangpeiqi Yi[1], Ludanni Li[1], Heng Zhai[1], Zihan Lu[1], Lu Jin[1], Jian R. Lu[3], Sheng Quan Xie[2], Zijian Zheng[4], Yi Li[1], Jiashen Li[1]**

[1]Department of Materials, The University of Manchester, Oxford Road, Manchester, M13 9PL, UK.

[2]School of Electrical and Electronic Engineering, University of Leeds, Leeds LS2 9JT, UK.

[3]Department of Physics & Astronomy, The University of Manchester, Oxford Road, Manchester, M13 9PL, UK.

[4]Institute of Textiles and Clothing, Research Institute for Intelligent Wearable Systems, Research Institute for Smart Energy, The Hong Kong Polytechnic University, Hong Kong S. A. R., China.

[*]Corresponding emails: henry.yili@manchester.ac.uk, jiashen.li@manchester.ac.uk

Abstract

A dramatic proliferation of research is placed on wearable and skin-mountable sensing devices because of the prominent serviceability in motion and health recognition, man-machine interaction, as well as artificial intelligence. State-of-the-art wearable sensors, however, lack sensing reliability towards either fickle wearable microclimate or multi-direction mechanical inputs, which leads to a suboptimal sensing accuracy throughout the implementation. In this work, we propose an assembly-flexible strain sensing network based on a carbon nanotube percolated configuration. The sensor possesses high reliability upon microenvironment change of wearable interfaces by taking advantage of the sensing stability in various temperatures, humidity, aqueous acid, and alkaline solutions. The response to bending, twisting, and pressuring is also marginal, guaranteeing sensing dependability against multi-direction mechanical inputs in practical wearable scenarios. By being integrated with deep learning and control

systems, the high-performance and biocompatible strain gauges can precisely identify hand gestures and manipulate the upwards/downwards bending of a robot wrist. It demonstrates huge potential in motion identification and man-machine interaction.

Keywords: Strain sensor; Carbon nanotube; Wearable interface; Sensing reliability; Wearable microclimate

1. Introduction

Wearable sensing devices with advanced wearing portability and real-time implementation show enormous potential in applications spanning from personal and public healthcare to motion identification and interaction, as well as artificial intelligence [1-3]. They overcome the drawbacks of conventional rigid sensors with poor flexibility and lightweight, as well as non-portability, arousing a technology revolution in next-generation electronics. Among various sensing mechanisms, the sensor based on resistance changes is very competitive due to the simple fabrication and high sensing performance [4]. Many active materials can be employed to develop this type of sensor such as metals [5], graphene [6, 7], carbonized fabrics [8, 9], and carbon nanotubes [10]. Cost-effective multi-wall carbon nanotubes (MWCNTs) are a critical candidate to fabricate on-skin flexible strain sensors by converting surface strain deformation into quantitatively analyzable digital signals. Even though previous works have reported the MWCNTs in strain sensor manufacture, the sensing elements in many of the devices with encapsulating configurations fail to form an open conductive network [11-14]. They also lack assembly flexibility to adapt to various planar and

curvilinear surfaces, which bring about inferior sensing serviceability.

Many efforts about wearable strain sensors have intensively been devoted to the improvement of sensitivity and sensing range [15, 16], while sensing reliability in actual applications is largely ignored. Most body motions at the time of strain deformations are also accompanied by bending, twisting, and/or pressuring inputs, instead of ideally monodirectional movements [17]. On the other hand, the microclimate of wearable interfaces often involves fickle temperature, humidity, and acid-base circumstances due to either body metabolism or the external environment inputs [18, 19]. Cutting-edge wearable strain sensors, however, have been always demonstrated out of the abovementioned practical scenarios. They possess a non-negligible response to multi-direction mechanical and environmental inputs, leading to suboptimal sensing reliability. To date, soft strain sensors are not reported with an emphasis on sensing reliability under multi-direction mechanical stimulations and environmental interference.

Herein, we propose a conductive percolation network through dispersing MWCNTs in Ecoflex for high-performance and soft strain gauges. The sensing networks with shape and pattern flexibility can be fabricated through wet spinning, 3D printing and stencil printing. The fiber-type sensor made with the Ecoflex/carbon nanotube composite (ECC) illustrates commendable linearity (r^2 = 98.92%) between applied strain and electrical response throughout the ultra-large sensing range (860%). Importantly, the

ECC fiber (ECCF) sensor possesses splendid machine washability and sensing reliability towards complicated wearable microclimate and multi-direction mechanical inputs. The biocompatible strain sensing device shows great potential in future artificial intelligence and man-machine interaction with remarkable sensing reliability.

2. Experimental Section

2.1. Dispersion of MWCNTs in Ecoflex, and preparation of the ECC sensors

MWCNTs (1.0 g) from Suzhou TANFENG Graphene Technology Co., Ltd were dispersed into 50 ml cyclohexane through ultrasonic treatment for 10 min. The maximum power output of the ultrasonic apparatus (SONICS, VCX 500) is 500 W, and we used 20% of the full load to run. Ecoflex (0050) solution A and B from SMOOTH-ON were added into the prepared CNT/cyclohexane respectively, then with another 10 min ultrasonic treatment under the abovementioned parameter. By changing the weight percentage of the Ecoflex, the ECC with desired performance can be implemented. In terms of the wet-spinning ECCF, the as-prepared ECC was filled into a syringe with the extrusion of a syringe pump, and the flow rate of the syringe pump is 0.1 mL/min. By changing the syringe needle, fiber diameter can be controlled. 3D printed ECC tracks were prepared using a 3D printing instrument purchased from Shenzhen TONGLI Co., Ltd. Sticky aluminum foil tape (3M Industrial) with piercing patterns was stuck onto fabrics, then the as-prepared ECC was printed on the fabric by stencil printing. Sample curing was performed in a hot oven (80 ℃) for 2 h, then cool in room condition overnight.

2.2. Morphology and structure characterization of the ECC sensors

We observed the surface and section morphology of the ECC sensors through either SEM (Quanta 250) or an optical microscope (Keyence VHX-5000). To clearly observe the distribution and network of MWCNTs inside the sensor, part of Ecoflex was removed from the composite fiber at a high temperature (500 ℃) in a tube furnace [18]. The element content and distribution were measured by the Quanta 250 SEM equipped with energy-dispersive X-ray spectroscopy (EDS). We investigated the adhesion force between the ECC and substrates via a tensile strength gauge (TOWA Industrial Co. Ltd). The force was recorded when the ECC separated from substrates at a steady speed. A Nicolet 5700 Fourier transform infrared spectrometer (Thermo Fisher Scientific), and a Raman spectrometer (Renishaw Invia) with a 633 nm laser wavelength were applied to characterize the corresponding spectrum features of the samples. We use a digital camera (Nikon D700, 105 mm/f2.8 D lens) to catch the water droplets on the ECCF16 sensor to show its hydrophobicity.

2.3. Evaluation of electromechanical performance and reliability

The sample resistance during performance evaluation was measured through a multifunctional electricity meter (Keithley 2000), while the applied scanning voltage in investigating static stability was supplied from another multimeter (Keithley 2450). The software matched with the two instruments was purchased from Beijing Hanlei Technology Co., LTD. Target mechanical inputs such as force and strain were carried

out via a universal material testing machine (Instron 3344L). Cyclic temperature and relative humidity were applied in a cabinet (Datacolor Conditione) to show the temperature and humidity independence. Three samples were used for obtaining the variable coefficient of mechanical performance and sensing performance to show the performance stability. Strong acid and alkaline solutions used in the investigation of pH stability are hydrochloric acid (1 mol/L) and sodium hydroxide (1 mol/L) solution respectively. We washed the ECCF16 sensor with a wash fastness tester system (Roaches, Washtec-P) according to the washing description in BS EN ISO 105 C06 A1S [20]. The fiber was surrounded by 25 stainless steel balls and Economic Commission for Europe reference detergent B (4 g/L) in the rolling wash process. The temperature and humidity in the homemade box were detected by a temperature and relative humidity indicator (SHT4x Smart Gadget).

2.4. Investigation of cell viability

Adult human dermal fibroblast (HDFa, skin cell-line, C-013-5C) was used to investigate the effect of the Ecoflex and Ecoflex/CNT samples on cell viability. Cell lines used in cytotoxicity tests concerning skin would be either human dermal fibroblast or human epidermal keratinocytes [21]. Although the device will not directly contact the dermis, dermal fibroblast can be used as a proxy for keratinocytes in cytotoxicity tests [22]. The HDFa fibroblasts were cultured at 37 °C under a 5% CO_2 atmosphere in an incubator using high-glucose Dulbecco's modified Eagle's medium (DMEM) supplemented with 10 vol% heat-inactivated fetal bovine serum (FBS), 100U of

Streptomycin-Penicillin and 0.25 μ/L Amphotericin B.

To study the cell viability, the Ecoflex and Ecoflex/CNT membranes were first cut into 0.5 cm^2 rectangles and placed at the bottom in separate wells in a 24-well plate. The membranes were then sterilized by immersing in ethanol for 1-2 h. The HDFa cells were then seeded into the 24-well plate with Ecoflex or Ecoflex/CNT membranes at a density of 5.0×10^4 per ml (1 ml per well). The culture medium and 100 vol% dimethylsulfoxide (DMSO) was used as negative control (live) and positive control (dead), respectively.

Live/dead assay was used to quantify and qualify the cell viability after different incubation times (24 h and 72 h). Briefly, after 24 h incubation, the cell medium was discarded. Fluorescent dyes including 2 μM Calcein-AM (staining live cells) and 1 μM Propidium Iodide (PI, staining dead cells) were dissolved in phosphate buffer saline (PBS). 1 ml of staining solution was added to each well and incubated for 15 min. The fibroblasts fluorescence images were taken using a Nikon Eclipse TE2000-U microscopy. Channels with an excitation wavelength of 488 nm and 493 nm were used for live cells and dead cells, respectively. Live and death cell images from the same population were merged and analyzed by Image J. The live and dead cell number was counted by Image J and the cell viability was calculated by the equation below.

$$\frac{\text{number of live cells}}{\text{number of live cells} + \text{number of dead cells}} \times 100\%$$

2.5. Wireless system and deep learning networks

The multi-channel wireless data transmission system was supplied by LinkZill Technology Co., Ltd (Hangzhou, China), including a Bluetooth-based signal processing unit (TruEbox), and visualization software (TruEbox-01RC) matched with a smartphone. The CNN architecture adopted in this study is based on LeNet-5. It is composed of two convolutional boxes, a dense layer and a softmax layer. Each convolutional box includes a convolutional layer, a batch normalization layer, a leaky ReLU layer, a max-pooling layer and a dropout layer. The kernel size and stride of the convolutional layer are set as 3 and 1, respectively. There are 16 kernels in the first convolutional layer, and 32 kernels in the second convolutional layer. There are 100 hidden units in the dense layer. The CNN is trained in a 32-sized mini-batch for 30 epochs via adaptive moment estimation. The dynamics learning rate is set as 0.001, the pool size of the max-pooling layer is set as 3, and the dropout rate is set as 0.25. For each gesture, the participant was asked to perform continuous cycle trails: the hand started from the initial neutral position, moved to the target gesture, moved back to the neutral position, and started again.

2.6. Pneumatic wrist exoskeleton for motion interaction

The wrist exoskeleton was developed by University of Leeds. The exoskeleton is designed to fit on the back of the user's forearm, and a mechanical hinge was placed coaxially with the biological joint of the wrist. A potentiometer was used to measure the rotation angle of the wrist. Two Festo fluidic muscles DMSP20 were placed in an

antagonistic configuration to actuate the exoskeleton, and two proportional regulators Festo VPPM-6L-V1 were used to regulate the pressure of fluidic muscles. The NI myRIO was used for data acquisition and sends voltage signals to control the valves. The graphical user interface and control software was designed on a host computer using Labview and Python. The high-level classification algorithm was developed in python to infer the remote wrist posture based on the data output of the soft brace and generate the reference angle profile for target categories: wrist flexion, neutral position, and wrist extension. A low-level PID controller was developed in Labview to control the exoskeleton to track the angle profile.

3. Results and Discussion

3.1. Assembly-flexibility of the ECC networks

The ECC is prepared through two simple steps: (1) dispersing MWCNTs into cyclohexane solvent with ultrasonic treatment to promote dispersion (Fig. 1a, Fig. S1a), and (2) mixing the cyclohexane solution with the MWCNTs inside into Ecoflex (A) and (B) respectively (Fig. S1b), and then blending them (Fig. 1b). The ECC shows high flexibility in the sensor assembly. Fig. 1c shows the fiber-type strain sensor through wet spinning (Movie S1), of which diameter is flexible to be managed from a diameter control pinhole. The as-prepared ECC in an injector is spun into fibers in hot water by a syringe pump (Fig. S1c, d). After further curing in a hot oven, the percolated MWCNTs in cross-linked Ecoflex form a conductive pathway (Fig. S1e, f). An ECC-based logo (The University of Manchester) is printed through a 3D printer (Movie S2),

and the conductive track acting as an interconnector enables to light up a LED (Fig. 1d). Fig. 1e and Fig. S2 display various ECC patterns on knitting and woven fabrics respectively via stencil printing. With increasing elongation, the self-adhesive ECC deforms along with the stretching of the knitting textile substrate. The adhesion interface is very stable to endure hand friction and washing without visible degeneration (Movie S3).

3.2. Characterizations of the ECC

We investigate the MWCNT-percolated networks in determining electromechanical properties by taking the ECCF sensors as examples. The ECCFs with the mass ratios (Ecoflex to MWCNTs) of 18:1, 16:1, and 14:1 are denoted as ECCF18, ECCF16, and ECCF14 respectively. Fig. 2a depicts the surface morphology and the element distribution of the ECCF16 extruded through a pinhole with a diameter of 0.6 mm, indicating the uniformly distributed MWCNTs in the fiber surface. Also, such a homogeneous configuration can be observed in the fiber section (Fig. 2b). We remove part of Ecoflex to observe the distribution of MWCNTs in the composite. Ecoflex and MWCNTs are put into a combustion boat (Fig. S3a) and then treat at a high temperature. Ecoflex melts and MWCNTs maintain intact (Fig. S3b). By taking advantage of this, Ecoflex was partly removed from the composite fiber to expose, MWCNTs with a good distribution and a well-connected network (Fig. S3c, d). By changing the diameter control pinhole, it is very flexible to spin the ECCFs with miscellaneous thickness (Fig. S4). It should be noted that the fibers extruded from the pinhole diameter of 0.22 mm,

0.41 mm, and 0.60 mm acquire true diameters of 0.33 mm, 0.46 mm, and 0.66 mm, respectively. Corresponding expansion rates reach 150%, 112%, and 110%. It manifests a low spinning rate enables to decrease the fiber expansion in diameters. The amount of each component in the ECCFs does not deteriorate the even distribution of the MWCNTs, while higher Ecoflex content (ECCF 18) results in a smoother surface (Fig. S5). The pure Ecoflex (Fig. S6a) is rich in C, O, and Si (Fig. S6b), while the assembly of MWCNTs does not change the composition of elements. Fig. S6c reveals the surface element content of the ECCFs with varying proportions, where the C monotonously declines with a higher percentage of Ecoflex. The as-fabricated fibers can be knotted, and it still maintains conductive by tying a knot between two separated fibers (Fig. S7a). The fibers can also be connected by the uncured composite or direct knotting, and more importantly, the connected fibers are capable of withstanding a strain deformation of 100% (Fig. S7b).

Fig. 2c shows that the conductivity of the ECCFs improves as a function of enhancing the content of MWCNTs, where the resistivity of the ECCF14, ECCF16, and ECCF18 is 0.07, 0.13, and 1.54Ω·m respectively. Corresponding resistances in 10 cm length are 20, 39, and 450 kΩ. FTIR spectra of the ECC, MWCNTs and Ecoflex in Fig. 2d show that there is a significant difference at 785 cm^{-1}, which corresponds to the increase of C-Si bond [23]. The formation of the chemical bonds between MWCNTs and Ecoflex is of prime importance to the stability of the conductive networks. Raman spectrum of Ecoflex comprises an asymmetric peak at 489.5 cm^{-1}, explaining the existence of Si-O-

Si (Fig. S8). By contrast, there are two peaks at 1325.5 and 1587.1 cm^{-1} for the ECC and MWCNTs, which refer to the D bands and G bands of the MWCNTs. By directly printing the as-prepared ECCF onto flexible substrates, there is high adhesion between the ECCF and substrates. To quantitatively evaluate the interfacial strength, we investigate the multi-direction separating force between the printed ECCF and the woven fabric substrate (Fig. 2e). The force reaches as high as 0.24, 0.20, 0.18 and 0.19 N when the tensile direction is drawn at angles of 45°, 90°, 135° and laterally 45°, respectively (Fig. 2f). It also acquires a similar interface strength when the substrate becomes a typing paper (Fig. S9). The high adhesive ability can vertically suspend a decoration with a weight of 9.5 g (Fig. 2g).

Good biocompatibility is crucial for wearable materials and devices considering the frequently involved on-skin scenarios. The Ecoflex and ECC demonstrate remarkable biocompatibility using the verification of adult human dermal fibroblast (Fig. 2h). It shows the images of human dermal fibroblasts cultured in the incubation medium with the control, DMSO, Ecoflex and ECC at day 1 and day 3 (see details in Experimental Section). Through the analysis by image segmentation, quantification of the live/dead-stained cells depicts that both the Ecoflex and ECC possess negligible cytotoxicity. There is no significant difference in live-cell percentage throughout the 3 days, indicating the ECC has good biocompatibility. Body area sensing based on the ECC electronics would not bring about biological damages at the cellular level.

3.3. Electromechanical performance and mechanism

The ECCF16 sensor reveals a wide sensing range with outstanding linearity between applied strain and relative electrical changes throughout the strain up to 860% (Fig. 3a), of which gauge factor (GF) and R^2 are 8.13 and 98.92% respectively. The GF and the fitting degree of the sensor are highly reproducible from sample to sample, of which variable coefficient is only 12.57%, and 8.89% respectively (Fig. 3a insert). The broad linear sensing performance is superior to that of reported sensors with linear sensing feature for the combination of sensitivity and range (Fig. 3b) [17, 24-36]. By contrast, the ECCF14 sensor enables to endure the maximum strain of 638%, with the GF and R^2 of 8.26 and 98.46% respectively (Fig. S10a), and the GF and the fitting degree are highly reproducible among samples (Fig. S10b). The GF and R^2 are 77.34 and 85.63% respectively for the ECCF18 sensor within the strain of 1354% (Fig. S10c). The variable coefficient of the GF and R^2 is 4.63% and 22.09% respectively (Fig. S10d), indicating there is a high consistency in sensitivity while low conformance in linear sensing. The breaking stress of the sensors reach around 1.5 MPa (Fig. S11). The difference in mechanical performance (revealed by variable coefficient) among samples shows high consistency in breaking strain and lower conformance in breaking stress.

Based on the evolution of sensing and mechanical performance, it finds that the increased content of MWCNTs deteriorates the stretchability, while it does not significantly affect the breaking stress. It could be understood that more MWCNTs in the percolation network prevent the crosslinking of Ecoflex, thus lowering the

elongation. The ECCF14 acquires a lower sensing range and a similar sensitivity compared to the ECCF16, in contrast to the ECCF18 with both high sensitivity and measuring range. However, the ECCF18 sensor fails to exhibit linear sensing feature throughout the detectable range. The ECCF16 sensor, therefore, owns combined merits in terms of acceptable sensitivity and wide-range linear sensing property. To further understand the relationship between applied strain and monotonically incremental electrical outputs, we demonstrate electrical models to show the sensing mechanism. The MWCNTs randomly arranged in the ECCF16 configuration with a series of straight segments are supposed to be many multiple curved lines combined with each other [37]. With increasing elongation, the sensor reveals a monotonous decline in diameter size (Fig. 3c). Fig. 3d demonstrates the electrical model of the sensor without stretching, where the conduction pathway relies on direct contact and tunneling effect among interconnected and adjacent MWCNTs. After sufficient tensile deformation, the conductive percolation pathway maintains in the same manner, while the contact and tunneling resistance among segmented lines enlarge as a function of stretch-induced inclination and separation (Fig. 3e). It explains the crescent electrical outputs with applied strain deformation.

The wide sensing range and high-linearity ECCF16 sensor reveal outstanding electromechanical properties. Fig. 3f shows voltage-current curves of the sensor under various strains by applying a voltage from 0 to 5 v, manifesting the static resistance stability. By applying a cyclic loading-unloading strain from 0-50% with step-by-step

frequency (0.05-0.4 Hz), corresponding relative resistance changes in Fig. 3g are stable throughout with minor fluctuation. The response to dynamic strain stimulation is also reproducible (Fig. 3h). The noticeable recovery deterioration for the high-degree deformation (i.e., 640% strain) can be ascribed to the hysteresis caused by the viscoelasticity of Ecoflex (Fig. 3i). It enables to remedy the mismatch in electrical and mechanical shape by decreasing the deformation (Fig. S12a) or lowering the applied loading-unloading speed [8]. However, the inherent hysteresis for stretchable strain sensors cannot be completely dislodged. To evaluate the response speed, a quasi-transient step strain was applied to the sensor with a speed of 16.6 mm/s. The electrical signals in Fig. 3j indicate the response speed reaches around 54 ms, which meets the need of most wearable detections. Fig. 3k shows the relative electrical change by imposing periodic strain up to 6% with the frequency of 0.5 Hz for 2000 cycles. It is very stable in this range. Subsequently, the signals of the sensor are still stable under the further cyclic strain of 100% at a frequency of 0.25 Hz for 1000 cycles (Fig. S12b). The overshoot at incipient cycles for the 100% strain can be attributed to the viscoelasticity of Ecoflex [8]. Even experiencing the cyclic strain at low and high deformations, no visible damage arises on the fiber surface (Fig. S12c).

3.4. Electrical stability and sensing reliability

The MWCNT-percolated networks with the formation of chemical bonds between MWCNT and Ecoflex show high stability to hostile environments and a low response to many mechanical inputs. Fig. 4a illustrates the images of a dynamic waterdrop rolling

down on the inclined fiber (37.8°). Even at a lower inclined angle (19.6°), the waterdrop either does not stay on the fiber (Fig. S13). It shows the fiber's hydrophobicity feature. The sensor was washed in a wash fastness tester system at various temperatures with steel balls inside to provide mechanical friction (Fig. 4b). The weight and resistance after each washing are highly consistent with marginal fluctuation (Fig. 4c), indicating the prominent laundry resistance of the sensor. The microclimate in wearable interfaces often has fickle temperature, humidity, even alkalinity, and acidity. To mimic the inputs of real-world wearable scenarios with wide-range temperature and humidity, we evaluated the stability of the sensor in a homemade device (Fig. S14) reported in our previous work [17]. Fig. 4d, e show the sensor response to cyclic loading strain of 20% in increasing temperature (27-45 ℃) and relative humidity (28-95%) respectively. There is an absence of temperature and humidity dependence. It is also proven by evaluating the relative resistance change (without deformation) in a cabinet by applying cyclic temperature (30-50 ℃) and relative humidity (20-85%). The electrical outputs further show the lack of dependence (Fig. S15). Fig. 4f exhibits the schematic diagram of measuring the sensor electrical performance in air, water, acid (pH = 1), and alkali solution (pH = 14). The relative change in resistance does not depend on the surroundings (Fig. 4g, and Movie S4), because only very limited MWCNTs on the surface are exposed to the environment. A majority of the MWCNTs are isolated due to the hydrophobicity and bonding structure in the conductive networks.

Wearable strain sensors do not ideally perform tensile strain deformation due to

multifarious mechanical inputs in real applications. The ECCF16 shows independence to bending and twisting, and very minor dependence on pressuring. The relative change in resistance does not show dependence on the cyclic bending from 0 to 90%. The bending is calculated through length change/initial length (%) of the fiber (Fig. 4h), which is reported in our previous work [17]. It indicates the sensor is insensitive to bending. Also, its response to the twist up to 720° is undiscerning (Fig. 4i) when applying periodic twisting by a programmable homemade device (Fig. S16). Fig. 4j depicts the pressuring test and corresponding electrical response. Gradually increasing pressure enlarges the resistance of the fiber because: the pressure-induced deformation at the fiber section deteriorates the electron transfer; the limited deformation fails to significantly promote the contact among MWCNTs due to its stable construction. However, the fractional resistance change just reaches approximately 10% under the force of 2 N. The force corresponds to the high pressure of 159 kPa (see the calculation in Fig. S17), beyond general wearable pressure (i.e., 100 kPa) [38]. The fiber sensor, therefore, maintains insensitive to pressure especially considering most of the deformation at the time low strain deformation seldom with high pressure in practical applications. Based on the abovementioned characterizations and demonstrations, the ECC sensors reveal conjunct assets including mounting flexibility, wide-range linear sensing feature, and sensing reliability in various temperature, humidity, and mechanical inputs, superior to state-of-the-art strain sensors (Table S1).

3.5. Motion identification and interaction

Taking advantage of the mounting flexibility, the high-performance ECC sensors are capable of being integrated with clothes through sewing and printing for motion identification and interaction. We fabricate a smart glove with five pieces of ECCF16 sensors sewn in each finger respectively (Fig. S18a). The metal buttons serve as electrodes at both ends of each sensor (Fig. S18b). The low resistance (0.1 Ω) of the button is negligible compared to the sensor resistance (Fig. S18c). The multi-channel electrical signals of the glove can be displayed in a personal smartphone through Bluetooth transmission (Fig. 5a, and Movie S5). Fig. 5b shows the electrical patterns via individually and successively bending the finger from the thumb to little. The outputs present a high synchronization with corresponding motions. Collected signals under repeated hand gestures (I-IV) are analyzed with a convolutional neural network (CNN) (Fig. 5c). Briefly, the recorded multi-channel data from sensors are filtered digitally using a sixth-order low-pass Butterworth filter to remove high-frequency noise. To extract samples for CNN, the 1.2 s sliding windows with 0.2 s increment are used to segment the data. The fast Fourier transform (FFT) is applied to each channel of the segmented data to obtain the spectrum of each window. The transformed data are randomly split into 80% and 20% for training and test set. With the step-by-step process and analysis, hand gestures (I-IV) can be recognized with a high precision of 98.4% (Fig. 5d). We believe the motion recognition system based on the high-performance sensor and high-accuracy algorithm can monitor and identify many other movements.

As a proof-of-concept demonstration of man-machine interaction, two ECC sensors are

individually mounted to a wrist band via stencil printing (Fig. 5e) to control the movement of a robot wrist. Importantly, the environmental temperature and humidity have less impact on the sensor's response (Fig. S19). It means that the sensor can reliably detect motions without the concerns of the body metabolism or surrounding environment inputs. Fig. 5f presents the sensors' response when the wrist slightly bends from the neutral position to the "down-back-up-back" condition. We show a motion interaction system to control the bend of the robot wrist for capturing the wrist posture. A pneumatic wrist exoskeleton (Fig. S20) for robot-assisted wrist exercise, a custom-made graphical user interface (Fig. 5g), and software are used for processing the data and controlling the exoskeleton. The data outputs from the band are classified into three categories: top sensor bending; neutral position; bottom sensor bending. It shows a high degree of accuracy of 99.3% (Fig. S21). Each of the wrist postures is assigned with a specific motor command of the exoskeleton that relates to wrist flexion, neutral position, the wrist extension, respectively. The human wearing the band can control the wrist movement of another human wearing the wrist exoskeleton, and supervise the wrist flexion/extension exercise (Movie S6). Such a motion interaction system shows potential in movement rehabilitation and physical therapy for human injury.

4. Conclusion

In summary, we have reported an assembly-flexible strain sensing network based on a MWCNT-percolated configuration, which can be implemented by wet spinning, 3D printing and stencil printing to adapt to various wearing surfaces. Taking advantage of

its hydrophobicity and stable percolation construction, the sensor is independent to various temperatures and humidity, liquid water, strong acid, and alkali solutions, and insensitive to the inputs of bending, twisting, and pressuring. It helps to improve sensing reliability towards volatile wearable microclimates and multi-direction mechanical fluctuation in practical applications. High-accuracy and multi-channel sensing networks based on the ECC sensors are successfully demonstrated to recognize hand gestures and control a robot wrist. We envision the biocompatible and high-performance strain sensing networks are promising for high-accuracy artificial intelligence and future communications.

Declaration of competing interest

The authors declare that they have no known competing financial interests or personal relationships that could have appeared to influence the work reported in this paper.

CRediT authorship contribution statement

Zekun Liu: Conceptualization, Methodology, Investigation, Data curation, Writing the original draft. Zhenhong Li: Methodology. Ludanni Li: Methodology. Heng Zhai: Investigation. Zihan Lu: Resources. Lu Jin: Data curation. Jian R. Lu: Methodology. Sheng Quan Xie: Methodology. Zijian Zheng: Supervision. Yi Li: Supervision, Funding acquisition. Jiashen Li: Conceptualization, Writing-review & editing, Supervision.

Acknowledgments

This work is financially supported by the EU Horizon 2020 through project ETEXWELD-H2020-MSCA-RISE-2014 (Grant No. 644268), The University of Manchester through UMRI project “Graphene-Smart Textiles E-Healthcare Network” (AA14512), Engineering and Physical Sciences Research Council (EPSRC) of UK under Grant EP/V057782/1.

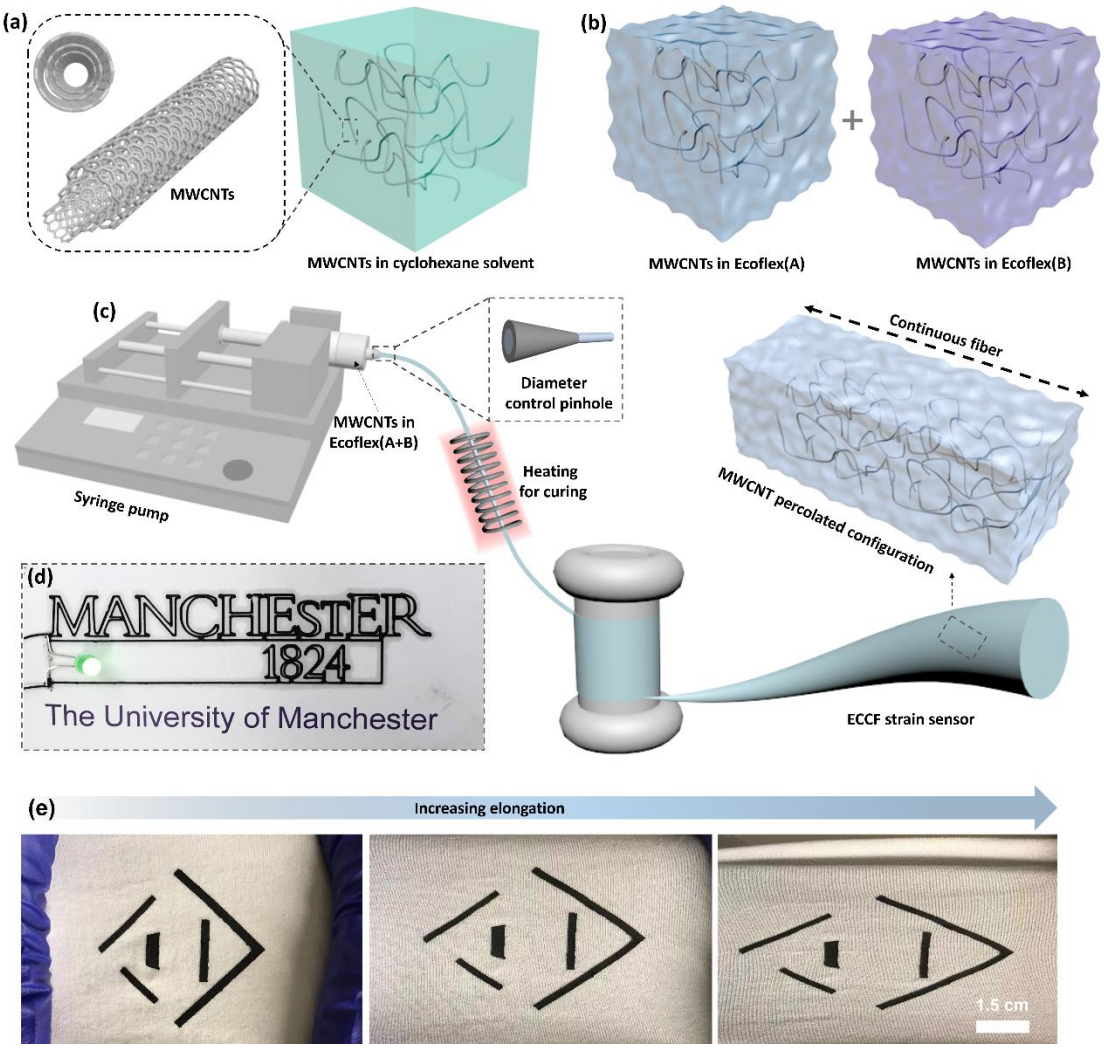

Fig. 1. MWCNT-percolated networks and the assembly flexibility. (a) Illustration of dispersing MWCNTs into cyclohexane solvent through ultrasonic treatment. (b) Blending the MWCNTs in cyclohexane with Ecoflex (A) and (B) respectively, and then

mixing them for following preparation of cured ECC. (c) Schematic diagram of the fabrication of the ECCF sensor by wet spinning. (d) A 3D-printed pattern (Manchester 1824) acted as an interconnector to light up a LED. (e) Photographs of the ECC pattern by stencil printing deforming along with the knitting fabric substrate.

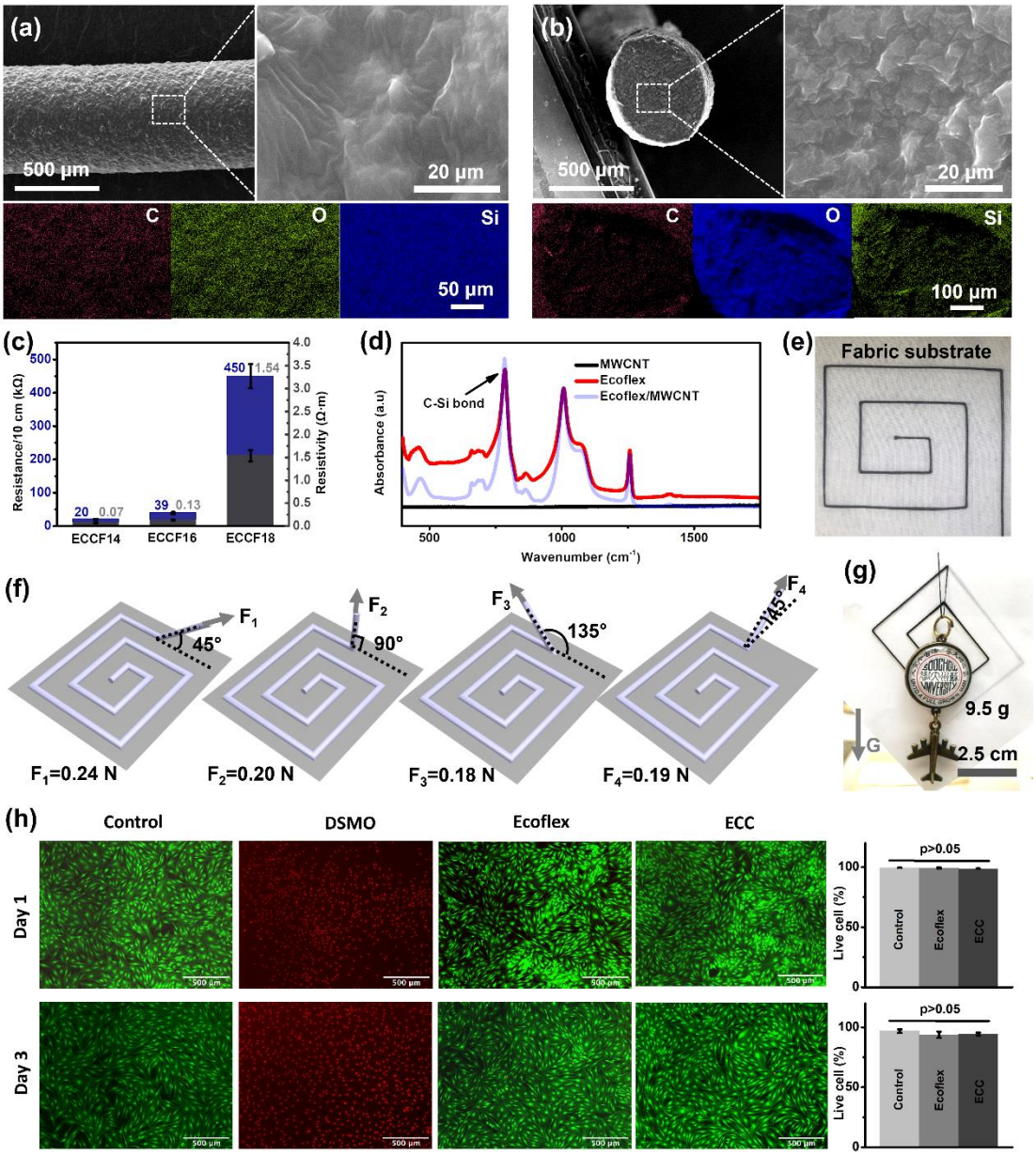

Fig. 2. Characterizations of the ECC. Morphology and element distribution of the ECCF16 at the (a) surface, and (b) section. (c) The conductivity of the ECCFs with

different MWCNT percentages extruded through a pinhole with a diameter of 0.6 mm. (d) FTIR spectra of the ECC, pure Ecoflex, and MWCNTs. (e) Image of a printed ECC track onto a piece of woven cotton fabric. (f) Illustration of tensile directions and corresponding separating forces, showing the good interfacial strength between the ECC and woven cotton fabric. (g) Image of an ECC track onto a typing paper to vertically suspend a decoration with the weight of 9.5 g. (h) Investigation of cell viability from live/dead cell assay, showing the good biocompatibility of the ECC.

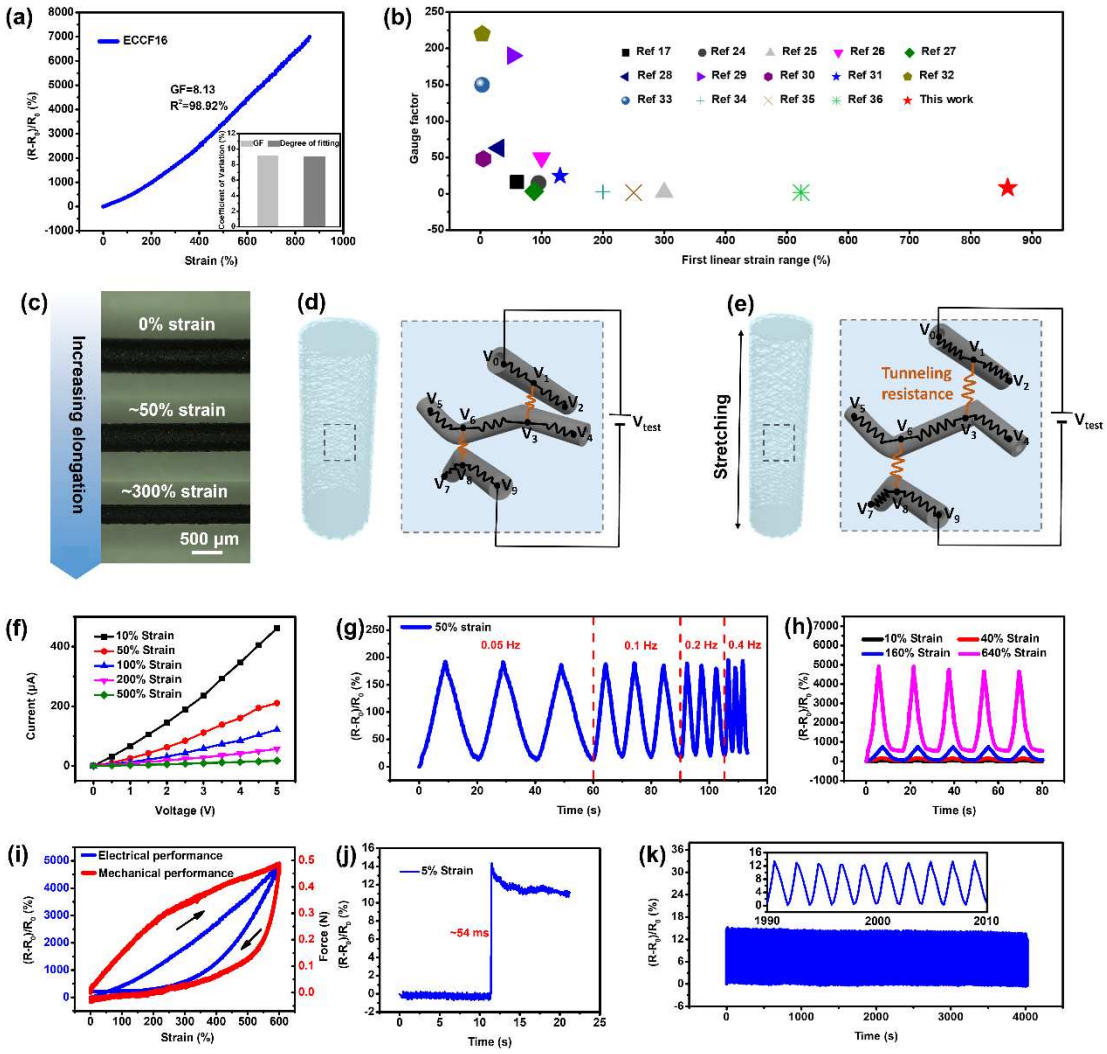

Fig. 3. Electromechanical performance and mechanism. (a) Calibration of the ECCF16

sensor. The insert is the variable coefficient of GF and fitting degree, showing the sensing performance reproducibility from sample to sample. (b) Comparisons between the ECCF16 sensor and reported strain sensor with linear sensing performance, showing the ultra-broad linearity. (c) Optic images of the ECCF16 under increasing elongation. Electrical models in (d) initial and (e) stretched states to show the sensing mechanism. (f) Voltage–current curves under various strains by applying a 0-5 v voltage, showing the resistance stability in static conditions. Dynamic stability of the ECCF16 sensor under various (g) frequencies, and (h) strains. (i) Electrical and mechanical outputs during a loading-unloading strain from 0 to 600%, showing the sensor hysteresis. (j) The electrical signals by applying a quasi-transient step strain of 5% with the speed of 16.6 mm/s, showing the fast response time. (k) Electrical signals at an applied cyclic strain of 6% with the frequency of 0.5 Hz for 2000 cycles.

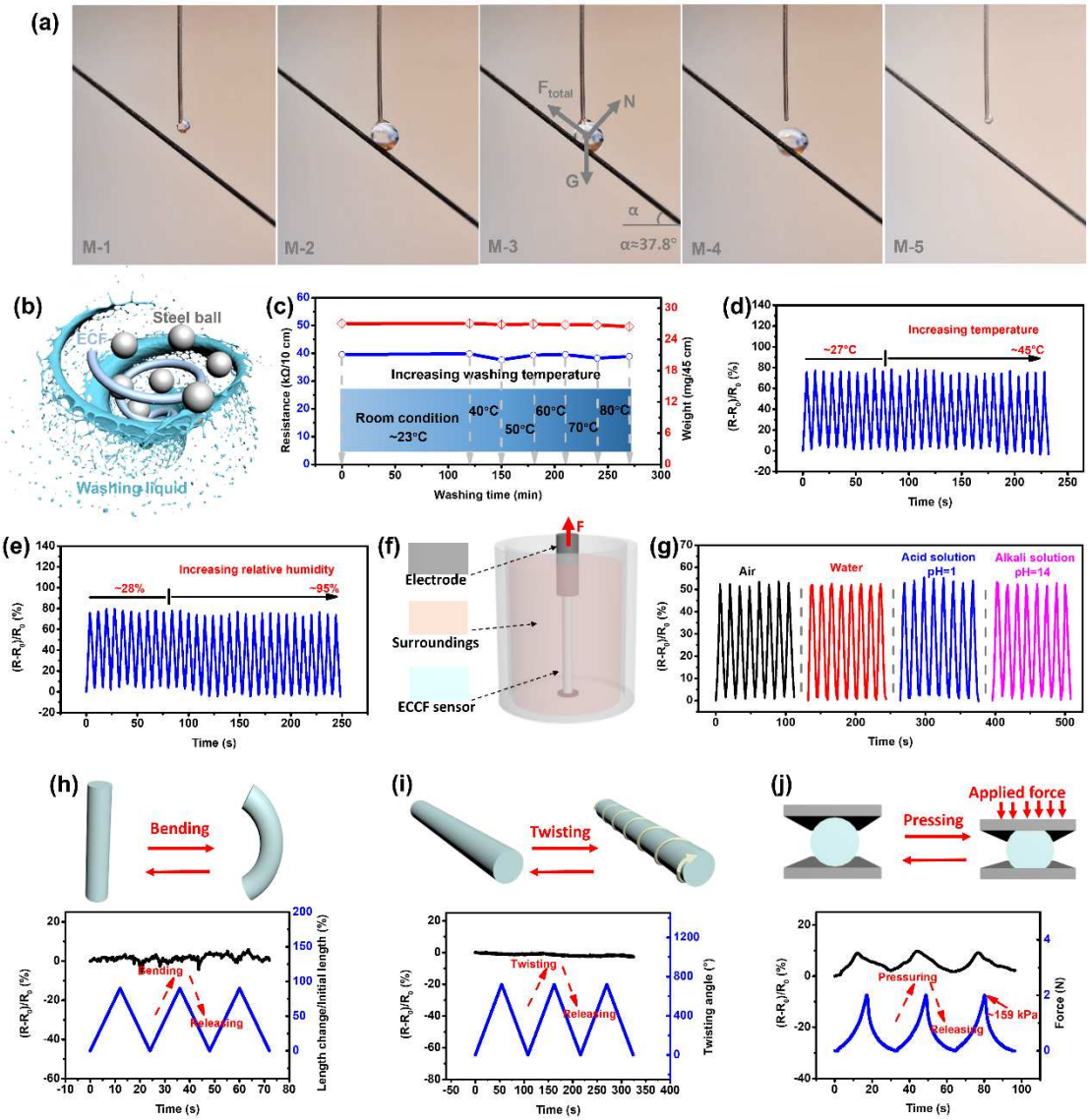

Fig. 4. Electrical stability and sensing reliability of the ECCF16. (a) Images of a water droplet rolling down on the inclined (37.8°) fiber, showing the hydrophobicity. The G refers to droplet gravity, N represents the normal force, and F_{total} is resistance in an inclined direction. (b) Illustration of machine-washing process. (c) The weight and resistance change during 270-min machine washing at various temperatures. Electrical outputs of the sensor under cyclic loading strain of 20% in (d) various temperatures, and (e) relative humidity, showing its temperature and humidity independence. (f) Illustration of measuring the sensor stability in air, water, acid, and alkali solution. (g)

The sensor responds to complex and harsh environments, showing its high reliability. Illustration, and relative electrical change of the sensor to (h) bending, (i) twisting, and (j) pressuring, showing its anti-jamming performance to the mechanical stimulation.

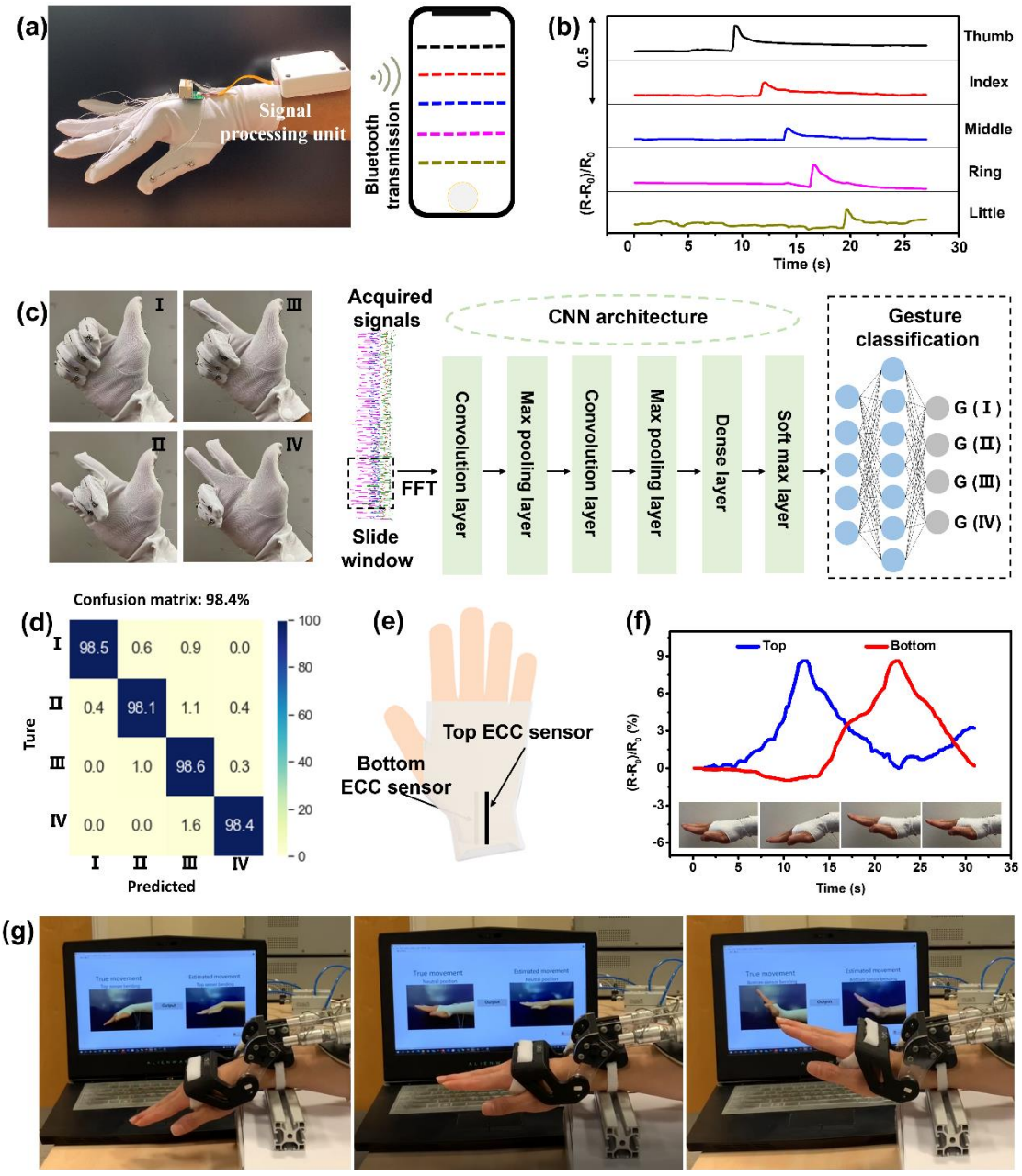

Fig. 5. Motion identification and interaction. (a) A smart glove with the fiber sensor sewn in each finger and data visualization through Bluetooth. (b) Normalized electrical signals from individually and successively finger bending from thumb to little. (c) Hand gesture identification by deep learning networks. (d) Confusion matrix of hand gesture

identification, showing its high degree accuracy of 98.4%. (e) Illustration of a wrist band with two ECC sensors through stencil printing. (f) Electrical outputs respond to continuous downwards and upwards wrist bending. Inserts are corresponding images at each stage. (g) Wrist bending rehabilitation system for remote robot-assisted exercises, showing the application in man-machine interaction.

References

[1] L. DeFrancesco, I. Jarchum, Focus on wearable sensors, Nat. Biotechnol. 4 (2019) 329.

[2] G.-H. Lee, H. Moon, H. Kim, G.H. Lee, W. Kwon, S. Yoo, D. Myung, S.H. Yun, Z. Bao, S.K. Hahn, Multifunctional materials for implantable and wearable photonic healthcare devices, Nat. Rev. Mater. 5 (2020) 149-165.

[3] Z. Liu, T. Zhu, J. Wang, Z. Zheng, Y. Li, J. Li, Y. Lai, Functionalized Fiber-Based Strain Sensors: Pathway to Next-Generation Wearable Electronics, Nano-Micro Lett. 14 (2022) 1-39.

[4] S. Seyedin, P. Zhang, M. Naebe, S. Qin, J. Chen, X. Wang, J.M. Razal, Textile strain sensors: a review of the fabrication technologies, performance evaluation and applications, Mater. Horiz. 6 (2019) 219-249.

[5] C. Zhu, R. Li, X. Chen, E. Chalmers, X. Liu, Y. Wang, B.B. Xu, X. Liu, Ultraelastic Yarns from Curcumin-Assisted ELD toward Wearable Human–Machine Interface Textiles, Adv. Sci. 7 (2020) 2002009.

[6] H. Zhai, L. Xu, Z. Liu, L. Jin, Y. Yi, J. Zhang, Y. Fan, D. Cheng, J. Li, X. Liu, Twisted graphene fibre based breathable, wettable and washable anti-jamming strain sensor for underwater motion sensing, Chem. Eng. J. 439 (2022) 135502.

[7] L. Xu, Z. Liu, H. Zhai, X. Chen, R. Sun, S. Lyu, Y. Fan, Y. Yi, Z. Chen, L. Jin, J.

Zhang, Y. Li, T.T. Ye, Moisture-Resilient Graphene-Dyed Wool Fabric for Strain Sensing, ACS Appl. Mater. Interfaces 12 (2020) 13265-13274.

[8] C. Wang, X. Li, E. Gao, M. Jian, K. Xia, Q. Wang, Z. Xu, T. Ren, Y. Zhang, Carbonized silk fabric for ultrastretchable, highly sensitive, and wearable strain sensors, Adv. Mater. 28 (2016) 6640-6648.

[9] Z. Liu, Z. Li, H. Zhai, L. Jin, K. Chen, Y. Yi, Y. Gao, L. Xu, Y. Zheng, S. Yao, A highly sensitive stretchable strain sensor based on multi-functionalized fabric for respiration monitoring and identification, Chem. Eng. J. 426 (2021) 130869.

[10] S.-S. Xue, Z.-H. Tang, W.-B. Zhu, Y.-Q. Li, P. Huang, S.-Y. Fu, Stretchable and ultrasensitive strain sensor from carbon nanotube-based composite with significantly enhanced electrical and sensing properties by tailoring segregated conductive networks, Compos. Commun. 29 (2022) 100987.

[11] M. Amjadi, Y.J. Yoon, I. Park, Ultra-stretchable and skin-mountable strain sensors using carbon nanotubes–Ecoflex nanocomposites, Nanotechnology 26 (2015) 375501.

[12] S. Zhang, L. Wen, H. Wang, K. Zhu, M. Zhang, Vertical CNT–Ecoflex nanofins for highly linear broad-range-detection wearable strain sensors, J. Mater. Chem. C 6 (2018) 5132-5139.

[13] Y. Xu, X. Xie, H. Huang, Y. Wang, J. Yu, Z. Hu, Encapsulated core–sheath carbon nanotube–graphene/polyurethane composite fiber for highly stable, stretchable, and sensitive strain sensor, J. Mater. Sci. 56 (2021) 2296-2310.

[14] N. Qaiser, F. Al-Modaf, S.M. Khan, S.F. Shaikh, N. El-Atab, M.M. Hussain, A

Robust Wearable Point-of-Care CNT-Based Strain Sensor for Wirelessly Monitoring Throat-Related Illnesses, Adv. Funct. Mater. 31 (2021) 2103375.

[15] Z. Liu, Z. Li, H. Zhai, L. Jin, K. Chen, Y. Yi, Y. Gao, L. Xu, Y. Zheng, S. Yao, A highly sensitive stretchable strain sensor based on multi-functionalized fabric for respiration monitoring and identification, Chem. Eng. J. (2021) 130869.

[16] K.-H. Kim, S.K. Hong, S.-H. Ha, L. Li, H.W. Lee, J.-M. Kim, Enhancement of linearity range of stretchable ultrasensitive metal crack strain sensor via superaligned carbon nanotube-based strain engineering, Mater. Horiz. 7 (2020) 2662-2672.

[17] Z. Liu, Y. Zheng, L. Jin, K. Chen, H. Zhai, Q. Huang, Z. Chen, Y. Yi, M. Umar, L. Xu, Highly Breathable and Stretchable Strain Sensors with Insensitive Response to Pressure and Bending, Adv. Funct. Mater. 31 (2021) 2007622.

[18] Z. Liu, K. Chen, A. Fernando, Y. Gao, G. Li, L. Jin, H. Zhai, Y. Yi, L. Xu, Y. Zheng, Permeable graphited hemp fabrics-based, wearing-comfortable pressure sensors for monitoring human activities, Chem. Eng. J. 403 (2021) 126191.

[19] Y. Yang, Y. Song, X. Bo, J. Min, O.S. Pak, L. Zhu, M. Wang, J. Tu, A. Kogan, H. Zhang, A laser-engraved wearable sensor for sensitive detection of uric acid and tyrosine in sweat, Nat. Biotechnol. 38 (2020) 217-224.

[20] N. Karim, S. Afroj, S. Tan, P. He, A. Fernando, C. Carr, K.S. Novoselov, Scalable production of graphene-based wearable e-textiles, ACS Nano 11 (2017) 12266-12275.

[21] C. Wiegand, U.-C. Hipler, Evaluation of biocompatibility and cytotoxicity using

keratinocyte and fibroblast cultures, Skin Pharmacol. Physiol. 22 (2009) 74-82.

[22] A. Pullanchiyodan, L. Manjakkal, S. Dervin, D. Shakthivel, R. Dahiya, Metal coated conductive fabrics with graphite electrodes and biocompatible gel electrolyte for wearable supercapacitors, Adv. Mater. Technol. 5 (2020) 1901107.

[23] M. Vetter, I. Martın, A. Orpella, J. Puigdollers, C. Voz, R. Alcubilla, IR-study of a-SiCx: H and a-SiCxNy: H films for c-Si surface passivation, Thin Solid Films 451 (2004) 340-344.

[24] Q. Liu, J. Chen, Y. Li, G. Shi, High-performance strain sensors with fish-scale-like graphene-sensing layers for full-range detection of human motions, ACS Nano 10 (2016) 7901-7906.

[25] J. Zhou, Y.-L. Hsieh, Conductive polymer protonated nanocellulose aerogels for tunable and linearly responsive strain sensors, ACS Appl. Mater. Interfaces 10 (2018) 27902-27910.

[26] Z. Qin, X. Sun, Q. Yu, H. Zhang, X. Wu, M. Yao, W. Liu, F. Yao, J. Li, Carbon Nanotubes/Hydrophobically Associated Hydrogels as Ultrastretchable, Highly Sensitive, Stable Strain and Pressure Sensors, ACS Appl. Mater. Interfaces 12(2020)4944.

[27] Z. Li, X. Qi, L. Xu, H. Lu, W. Wang, X. Jin, Z.I. Md, Y. Zhu, Y. Fu, Q. Ni, Self-repairing, large linear working range shape memory carbon nanotubes/ethylene vinyl acetate fiber strain sensor for human movement monitoring, ACS Appl. Mater. Interfaces 12 (2020) 42179-42192.

[28] S. Yang, C. Li, X. Chen, Y. Zhao, H. Zhang, N. Wen, Z. Fan, L. Pan, Facile

Fabrication of High-Performance Pen Ink-Decorated Textile Strain Sensors for Human Motion Detection, ACS Appl. Mater. Interfaces 12 (2020) 19874-19881.

[29] Y. Yang, Z. Cao, P. He, L. Shi, G. Ding, R. Wang, J. Sun, Ti3C2Tx MXene-graphene composite films for wearable strain sensors featured with high sensitivity and large range of linear response, Nano Energy 66 (2019) 104134.

[30] J. Zhou, X. Xu, Y. Xin, G. Lubineau, Coaxial Thermoplastic Elastomer-Wrapped Carbon Nanotube Fibers for Deformable and Wearable Strain Sensors, Adv. Funct. Mater. 28 (2018) 1705591.

[31] K.H. Kim, N.S. Jang, S.H. Ha, J.H. Cho, J.M. Kim, Highly sensitive and stretchable resistive strain sensors based on microstructured metal nanowire/elastomer composite films, Small 14 (2018) 1704232.

[32] X. Liu, C. Tang, X. Du, S. Xiong, S. Xi, Y. Liu, X. Shen, Q. Zheng, Z. Wang, Y. Wu, A highly sensitive graphene woven fabric strain sensor for wearable wireless musical instruments, Mater. Horiz. 4 (2017) 477-486.

[33] X. Shi, S. Liu, Y. Sun, J. Liang, Y. Chen, Lowering Internal Friction of 0D–1D–2D Ternary Nanocomposite-Based Strain Sensor by Fullerene to Boost the Sensing Performance, Adv. Funct. Mater. 28 (2018) 1800850.

[34] D. Zhang, K. Zhang, Y. Wang, Y. Wang, Y. Yang, Thermoelectric effect induced electricity in stretchable graphene-polymer nanocomposites for ultrasensitive self-powered strain sensor system, Nano Energy 56 (2019) 25-32.

[35] X. Sun, Z. Qin, L. Ye, H. Zhang, Q. Yu, X. Wu, J. Li, F. Yao, Carbon nanotubes reinforced hydrogel as flexible strain sensor with high stretchability and

mechanically toughness, Chem. Eng. J. 382 (2020) 122832.

[36] G. Chen, H. Wang, R. Guo, M. Duan, Y. Zhang, J. Liu, Superelastic EGaIn composite fibers sustaining 500% tensile strain with superior electrical conductivity for wearable electronics, ACS Appl. Mater. Interfaces 12 (2020) 6112-6118.

[37] S. Jung, H.W. Choi, F.C. Mocanu, D.-W. Shin, M.F. Chowdhury, S.D. Han, Y.-H. Suh, Y. Cho, H. Lee, X. Fan, Modeling electrical percolation to optimize the electromechanical properties of CNT/polymer composites in highly stretchable fiber strain sensors, Sci. Rep. 9 (2019) 1-10.

[38] Y. Zang, F. Zhang, C.-a. Di, D. Zhu, Advances of flexible pressure sensors toward artificial intelligence and health care applications, Mater. Horiz. 2 (2015) 140-156.